HHS Public Access

Author manuscript

Sci Transl Med. Author manuscript; available in PMC 2020 July 01.

Published in final edited form as:

Sci Transl Med. 2019 August 21; 11(506): . doi:10.1126/scitranslmed.aaw7736.

Imaging-assisted nanoimmunotherapy for atherosclerosis in multiple species

Tina Binderup[1,2,#], **Raphaël Duivenvoorden**[1,3,#], **Francois Fay**[1,4,#], **Mandy M.T. van Leent**[1], **Joost Malkus**[1], **Samantha Baxter**[1], **Seigo Ishino**[1], **Yiming Zhao**[1], **Brenda Sanchez-Gaytan**[1], **Jun Tang**[1,5], **Giuseppe Carlucci**[5,6], **Serge Lyashchenko**[5,7], **Claudia Calcagno**[1], **Nicolas Karakatsanis**[1], **Georgios Soultanidis**[1], **Max L. Senders**[1,8], **Philip M. Robson**[1], **Venkatesh Mani**[1], **Sarayu Ramachandran**[1], **Mark E. Lobatto**[1,9], **Barbara A. Hutten**[10], **Juan F. Granada**[11], **Thomas Reiner**[5,7], **Filip Swirski**[12], **Matthias Nahrendorf**[12], **Andreas Kjaer**[2], **Edward A. Fisher**[13], **Zahi A. Fayad**[1,*], **Carlos Pérez-Medina**[1,14], **Willem J.M. Mulder**[1,8,15,*]

[1]Translational and Molecular Imaging Institute, Icahn School of Medicine at Mount Sinai, New York, NY, USA [2]Department of Clinical Physiology, Nuclear Medicine and & PET, and Cluster for Molecular Imaging, Department of Biomedical Sciences, Rigshospitalet and University of Copenhagen, Copenhagen, Denmark [3]Department of Nephrology, Radboud Institute for Molecular Life Sciences, Radboud University Medical Center, Nijmegen, The Netherlands [4]Institut Galien Paris Sud, Faculté de Pharmacie, CNRS, Univ. Paris-Sud, Université Paris-Saclay, Châtenay-Malabry, France [5]Department of Radiology, Memorial Sloan Kettering Cancer Center, New York, NY, USA [6]Bernard and Irene Schwarz Center for Biomedical Imaging, New York University, New York, NY, USA [7]Department of Radiology, Weill Cornell Medical College, New York, NY, USA [8]Amsterdam University Medical Centers, Dept. of Medical Biochemistry, University of Amsterdam, Amsterdam, The Netherlands [9]Department of Radiology, Spaarne Gasthuis, Haarlem, The Netherlands [10]Department of Clinical Epidemiology, Biostatistics and Bioinformatics, Amsterdam University Medical Centers, Amsterdam, the Netherlands [11]CRF Skirball Center for Innovation, The Cardiovascular Research Foundation, Orangeburg, NY, USA [12]Center for Systems Biology and Department of Radiology, Massachusetts General Hospital, Harvard Medical School, Boston, MA, USA [13]Department of Medicine (Cardiology) and Cell Biology, Marc and Ruti Bell Program in Vascular Biology, New York University School of Medicine, New York, NY, USA [14]Centro Nacional de Investigaciones Cardiovasculares Carlos III, Madrid,

[*]Address correspondence to: Willem J.M. Mulder, willem.mulder@mssm.edu, Zahi A. Fayad, zahi.fayad@mssm.edu, Translational and Molecular Imaging Institute, Icahn School of Medicine at Mount Sinai, One Gustave L. Levy Place, Box 1234, New York, NY 10029, USA.

[#]Equal contribution

Author contributions: W.J.M.M. conceptualized and designed the study. T.B., R.D. and F.F. coordinated experimental planning and execution. F.F., B.L.S-G., Y.Z., J.T. and C.P.M. developed, synthesized, characterized and labeled the nanoimmunotherapy. M.E.L., F.F. and M.L.S. developed the rabbit model, and J.F.G. developed the swine model. T.B., R.D., M.M.T.L., J.M., S.I., S.B. and M.L.S. conducted the *in vivo* experiments. G.C., S.L. and T.R. produced FLT. C.C., V.M., M.E.L., P.M.R. and Z.A.F. developed the imaging protocols. S.I., C.C., T.B., N.K., G.S. and S.R. developed and performed image analysis. B.A.H. performed statistical analysis. M.N. and F.S. developed flow cytometry protocols and provided immunology insights. A.K., E.A.F. and Z.A.F. interpreted data and provided critical feedback. C.P.M. and W.J.M.M. wrote the manuscript, and T.B., C.P.M. and W.J.M.M. produced the figures. All the authors reviewed and provided feedback on the manuscript.

Competing interests: The authors declare no competing interests.

Data and materials availability:

Spain [15]Laboratory of Chemical Biology, Department of Biomedical Engineering and Institute for Complex Molecular Systems, Eindhoven University of Technology, Eindhoven, The Netherlands

Abstract

While the nanomedicine research field produces hundreds of studies every year, very few formulations have been approved for clinical use, due in part to nanomedicine's reliance on mouse studies. In this study, we report the escalation of a nanoimmunotherapy from mouse to large rabbit and porcine atherosclerosis models, with an emphasis on the solutions we implemented to overcome production and evaluation challenges. Specifically, we integrated translational imaging readouts within the workflow to both analyze the nanoimmunotherapeutic's *in vivo* behavior and assess treatment response in larger animals. We observed our nanoimmunotherapeutic's anti-inflammatory efficacy in mice as well as rabbits and pigs. Importantly, in the larger animal models, nanoimmunotherapeutically reduced inflammation halted plaque progression, underlining the approach's translatability and potential to acutely treat atherosclerosis.

Introduction

The nanomedicine research field continues to grow, with hundreds of new nanoformulations reported every year. However, comparatively few formulations are clinically translated to benefit patients. Indeed, the overwhelming majority of preclinical work is limited to proof-of-concept mouse studies, and serious concerns have been raised about these studies' relevance, particularly in relation to efficient nanomedicine drug delivery in patients (1). At the same time, a paradigm shift in the nanomedicine field has gained momentum as new nanotherapies are being designed to deliberately engage the immune system (2, 3) rather than evading it, which has been nanomedicine's primary focus for decades. The ability to selectively modulate the immune response via nanomedicines (4, 5), *i.e.* nanoimmunotherapy, is reinvigorating the field. This approach can treat conditions, such as cancer, atherosclerosis or autoimmune diseases, in which a dysregulated immune response is either an underlying or contributing factor. In the last decade, we have pioneered nanoimmunotherapeutic approaches to treat atherosclerosis, a chronic inflammatory disorder of medium and large arteries that is the major underlying cause of cardiovascular disease. We developed a myeloid cell-specific nanoimmunotherapy that rapidly and efficiently silences vessel wall inflammation (6) by inhibiting macrophage proliferation (7).

Such nanoimmunotherapies can be translationally significant if two key challenges are addressed. First, orders of magnitude more nanomaterial must be produced for larger animals and humans than for mice. Producing multigram amounts in a controlled and reproducible manner requires developing alternatives to traditional benchtop formulation methods. Second, the significantly lower number of large animals that can be reasonably included in a translational study necessitates different therapeutic readouts than those typically used in mouse studies. Concurrently, successful translation crucially requires developing both techniques to quantitatively determine the nanoimmunotherapeutic's

distribution in the body after administration and related non-invasive imaging methods to probe this over time (8).

Here, we report a strategy that surmounts the aforementioned translation hurdles to close the daunting gap between benchtop and bedside nanomedicine research. Our approach involves scaling up a nanoimmunotherapeutic production strategy using a microfluidizer-based high-pressure homogenization process and its imaging-guided evaluation in three different atherosclerosis animal models. After establishing the high-pressure homogenization-produced nanoimmunotherapy's efficacy in atherosclerotic mice, we perform non-invasive assessments of its *in vivo* behavior and treatment response in atherosclerotic rabbits and pigs by integrated positron emission tomography (PET) magnetic resonance imaging (MRI). We thus demonstrate the translatability of our nanoimmunotherapeutic approach and its ability to acutely treat vessel wall inflammation in atherosclerosis.

Results

Development and production scale-up of S-HDL nanoimmunotherapy

In two recent publications, we reported the development of a simvastatin-loaded high-density lipoprotein (S-HDL) nanotherapeutic that we successfully applied in atherosclerosis mouse models to treat vessel wall inflammation (6, 7). However, due to its low production rate (120 mg/hour), our original benchtop sonication-based S-HDL production method was not suitable for producing the necessary amounts for studies in large animal models. Therefore, we designed and implemented a high-pressure homogenization process, including innovative purification methods, to scale up S-HDL production, and generate the required amounts (Figure 1a).

We first implemented a large-scale apolipoprotein A1 (APOA1) extraction method. Using the optimized workflow described in the methods section, we isolated 10 g of APOA1 from purified human HDL, which is one order of magnitude more than we typically generate. Our previously reported benchtop S-HDL formulation method involves hydrating a film composed of phospholipids and simvastatin with a buffered APOA1 solution, followed by 1 hour of sonication and multiple purification steps (6, 7). The new production method also uses the formation of a dry film, albeit one containing at least 40 times more phospholipid/simvastatin. After the film's complete hydration with 0.5 L of an APOA1-containing saline buffer in the appropriate ratio, the suspension was homogenized using a microfluidizer 110-S Processor (Microfluidics, Newton, MA). This high-pressure homogenization method processes batches containing 5 g of total bulk ingredients in 30 minutes, leading to an 80-fold higher production rate compared to our original method. Due to the large amount of S-HDL produced, we scaled the purification steps using tangential flow filtration and funnel vacuum filtration methods. This process enabled the production of up to 18 g (total bulk ingredients) of S-HDL per production run, with a simvastatin recovery of 67 ± 6% (n=8, Table S1), yielding discoidal S-HDL particles (see TEM images in Figure 1a and Figure S1a) with a mean diameter of 23.6 ± 3.7 nm (dispersity index: 0.24 ± 0.04, n=8). These morphological features are comparable to S-HDL prepared using our original benchtop method (6, 7). We produced a total of approximately 90 g of S-HDL

nanoimmunotherapeutic with suitable physicochemical properties for *in vivo* application. (An overview of all individual batches' physicochemical properties is provided in Table S1).

To assess our nanoimmunotherapeutic's biodistribution and pharmacokinetics, we developed a ^{89}Zr-labeled S-HDL analog ([^{89}Zr]-S-HDL) following a strategy previously reported by us (9). In short, we included the phospholipid chelator DSPE-DFO in the formulation to allow radiolabeling with ^{89}Zr. Radiolabeling was performed by reacting with [^{89}Zr]zirconium (IV) oxalate, and radiochemically pure [^{89}Zr]-S-HDL (Figure S1b) was obtained in high yield (>85%). The radiolabeling allowed localization of our nanobiologic by *in vivo* PET imaging.

S-HDL's biodistribution, targeting and therapeutic efficacy in Apoe$^{-/-}$ mice

In two previously reported studies, we extensively evaluated benchtop-produced S-HDL's therapeutic efficacy in atherosclerotic apolipoprotein E deficient (*Apoe*$^{-/-}$) mice (6, 7). To ensure the S-HDL produced in large batches by high-pressure homogenization exerts similar therapeutic effects, we first conducted mouse experiments. We studied [^{89}Zr]-S-HDL biodistribution and pharmacokinetics in *Apoe*$^{-/-}$ mice that had been fed a Western diet for 12 weeks to induce advanced atherosclerosis. The blood radioactivity half-life was 3.1 hours (Figure 1c; two-phase decay, weighted $t_{1/2}$), which is comparable to the blood half-life of other HDL nanobiologics (2). PET imaging at 24 hours post injection showed [^{89}Zr]-S-HDL's accumulation in the spleen, kidneys, liver and periaortic lymph nodes (Figure 1d). PET imaging data were complemented by *ex vivo* gamma counting results (Figure 1e). Importantly, digital autoradiography of excised aortas revealed high radioactivity deposition in the aortic arch and roots, indicating high accumulation of our nanoimmunotherapy in atherosclerotic lesions (Figure 1e).

Subsequently, we investigated the anti-atherosclerotic efficacy of the S-HDL formulation produced by high pressure homogenization in *Apoe*$^{-/-}$ mice with advanced atherosclerosis. As readouts, we combined whole aorta flow cytometry (Figure 1f) and histological analysis of cross sections of the aortic arch, which is where plaque development is most reproducible in this mouse model. We found that four infusions of S-HDL (Simvastatin dose 60 mg/kg) within 1 week decreased aortic macrophage numbers by 45% (P<0.05, Figure 1g). Representative images from aortic arch histological sections are shown in Figure 1h. Collectively, these results demonstrate that microfluidizer-produced S-HDL's biodistribution, targeting and therapeutic efficacy mirror those of traditional S-HDL (7). This marks an important advancement, since production scale-up is a prerequisite for translation to large animal models and, ultimately, the ability to conduct human studies.

S-HDL nanoimmunotherapy translation to large animal models of atherosclerosis

The results of our mouse model experiments incentivized us to proceed with testing S-HDL in large animal models of atherosclerosis, namely rabbit and porcine models. Both are well-established atherosclerosis models in which plaque development is induced by a combination of Western diet and surgical denudation of the endothelium, resulting in accelerated plaque development (Figure 2a). In the rabbit model, aortic angioplasty was performed, whereas in the swine model lesions were induced in the femoral arteries. The therapeutic dose was calculated from human equivalent dose FDA tabulated values (10)

based on body weight and surface area. Drawing on our previous studies in mice, we used 60 mg simvastatin/kg body weight (180 mg/m^2) as a starting point and applied a ratio between correction factors (Km) of the different species. The calculated rabbit and pig doses were 15 (Km ratio = ¼) and 7.5 (Km ratio = 1/8) mg/kg, respectively.

Our translational evaluation encompassed PET imaging of biodistribution and plaque targeting (Figure 2b–f) and a non-invasive imaging-based assessment of treatment response (Figures 3 and 4). These protocols were developed and evaluated in a separate cohort of six pigs not included in the ensuing biodistribution and therapeutic experiments. Protocol development included optimizing imaging parameters for a) non-contrast-enhanced time-of-flight (TOF) MR angiography to identify the aorta and femoral arteries; b) 3-dimensional (3D), isotropic, high-resolution black blood vessel wall MRI for plaque quantification in the whole femoral arterial tree; c) 3D black blood dynamic contrast-enhanced (DCE) MRI with high spatial resolution and coverage to quantify plaque endothelial permeability. Specifically, flip angle and number of imaging slabs were varied for TOF angiography until adequate coverage and blood pool contrast were obtained. For 3D black blood vessel wall and DCE MRI, the acquisition plane, number of acquired slices, spatial resolution and number of signal averages were optimized to obtain high signal-to-noise ratios and minimize blood pool signal for adequate vessel wall delineation.

PET imaging of S-HDL's in vivo behavior in atherosclerotic rabbits and pigs

First, we performed *in vivo* PET/CT imaging to assess biodistribution and pharmacokinetics in atherosclerotic rabbits and pigs. Rabbits (n=2) and pigs (n=2) were infused with [^{89}Zr]-S-HDL. One rabbit and one pig were co-injected with DiD-S-HDL to validate targeting *ex vivo*. Whole-body static scans were acquired 1, 24 and 48 hours post injection. Images were initially dominated by a high blood-pool signal (1 hour), followed by liver and intestinal accumulation (24 and 48 hours), consistent with hepatobiliary excretion (Figure 2c). The clearance kinetics (Figure S2a) and radioactivity distribution pattern were similar in both species, with liver and kidneys as the main accumulation sites (Figure 2d).

After the last PET/CT scan (48 hours post injection), PET/MRI was performed in [^{89}Zr]-S-HDL-injected rabbits and pigs to assess plaque targeting *in vivo*. Clear focal vessel wall accumulation in rabbits' abdominal aortas and pigs' femoral arteries was visualized (Figure 2e). In these regions, radioactivity concentration was more than two-fold higher than in uninjured arterial fragments (Figure 2e). We performed near-infrared fluorescence (NIRF) imaging with DiD-S-HDL (1 rabbit and 1 pig) and Evans Blue (1 rabbit and 1 pig) to evaluate plaque targeting and vessel wall permeability, respectively. The corresponding arterial samples were compared against [^{89}Zr]-S-HDL autoradiography. DiD-S-HDL and [^{89}Zr]-S-HDL were co-localized in plaque (Figure 2f), whereas [^{89}Zr]-S-HDL and Evans Blue (Figure S2b) had a different distribution pattern in both rabbit and pig samples, revealing that HDL nanobiologics' accumulation in the vessel wall is not merely governed by microvessel permeability. The discrepancy between Evans blue and HDL nanobiologics' accumulation patterns corroborates our previous observations (11) that HDL nanobiologics' plaque accumulation is due to their inherent avidity for macrophages (6, 7, 9, 11).

PET/MR imaging of S-HDL's anti-atherosclerotic activity

Next, we investigated the efficacy of S-HDL therapy in large animal atherosclerosis models. Rabbits and pigs received four intravenous S-HDL infusions using simvastatin doses of 15 and 7.5 mg/kg, respectively. The infusions were given over the course of 2 weeks. We evaluated therapeutic response non-invasively and longitudinally using a multiparametric PET/MR imaging protocol (Figure 3a; details are presented in the Methods section). Four different atherosclerosis-related parameters were measured, namely (**i**) vessel wall inflammation by ^{18}F-FDG-PET, (**ii**) cellular proliferation by ^{18}F-FLT-PET, (**iii**) vessel wall permeability by *in vivo* DCE MRI (and *ex vivo* by Evans Blue NIRF imaging), and (**iv**) vessel wall thickness by T2-weighted MRI. Imaging sessions were performed at baseline and 2 weeks after the onset of therapy. Imaging was performed on the aorta in rabbits and the femoral arteries in pigs.

We used a linear mixed model (LMM) to statistically analyze differences in imaging-derived parameters between treatment groups. The imaging parameter at the end of the study (terminal scan) was used as the dependent variable. Type of treatment and imaging parameter at the start of the study (baseline) were defined as fixed effects, and the side (left or right femoral artery in pigs) as a random effect. Based on this analysis, vessel wall inflammation, as measured by ^{18}F-FDG-PET (Figure 3b), was not different between the S-HDL and placebo groups (LMM P=0.292 for rabbits, P=0.372 for pigs, Figure S3). A trend towards reduced cellular proliferative activity in the vessel wall as assessed by PET imaging of ^{18}F-FLT uptake (Figure 3c) was observed in rabbits and pigs treated with S-HDL (LMM P=0.146 for rabbits, P=0.086 for pigs, Figure S3). S-HDL did not affect vessel wall permeability in rabbits and pigs, as measured both *in vivo* by DCE-MRI (Figure 4a; LMM P=0.219 for rabbits, P=0.292 for pigs, Figure S3) and *ex vivo* by Evans Blue NIRF imaging (Figure 4b). Importantly, the most significant results were related to vessel wall thickness as assessed by T2-weighted-MRI. In rabbits, we observed significantly reduced vessel wall area in the abdominal aortas of S-HDL treated animals compared to controls (Figure 4c, top; LMM P=0.001, Figure S3), whereas in pigs, S-HDL treatment significantly halted vessel wall enlargement as compared to untreated animals (Figure 4c, bottom; LMM P=0.036, Figure S3). Representative histological sections from rabbit and porcine specimens are shown in Figure S4.

Overall, in rabbits we observed decreased imaging marker values in 74% of terminal scans with respect to baseline in the S-HDL group, while in the placebo group we noted increased values in 58% of the scans (Figure 4d). The median change between scans for the measured imaging parameters in the S-HDL group was −12.8% [interquartile range (IQR): −27.1 – 1.8 %], which was significantly different from that in the placebo group (Median: 6.6% [IQR: −14.3 – 23.4 %], P=0.005) (Figure 4e). Similarly, in pigs we observed elevated imaging marker values in 69% of terminal scans compared to baseline in the placebo group, with exactly the same proportion of scans showing decreased values in the S-HDL group (Figure 4f). The variation in the monitored imaging markers was significantly different between groups (Median placebo: 12.1 % [IQR: −3.9 – 28.0 %] versus median S-HDL: −7.7% [IQR: −22.5 – 0.9 %], P=0.01) (Figure 4g). A combined representation of the variation in all

imaging markers as a result of treatment in individual rabbits and pigs can be found in Figure S5.

S-HDL toxicity evaluation in pigs

Blood samples from pigs in both treatment groups were collected at the end of the study and analyzed for general biochemistry (Table 1) and complete blood count (Table 2) analysis. Liver enzymes (ALP, ALT, AST and GGT) and bilirubin concentrations were unaffected by S-HDL treatment. Interestingly, S-HDL treatment did not affect blood cholesterol concentration (P=0.80), confirming that S-HDL's effects are independent of simvastatin's cholesterol-lowering properties. The other analyzed parameters had no significant differences between the two groups except for decreased blood glucose concentration in the S-HDL-treated animals (P=0.03). Complete blood count results showed no difference in red blood cell, white blood cell, neutrophil, lymphocyte or monocyte numbers. However, the neutrophil compartment was reduced (P=0.03) while the lymphocyte compartment expanded (P=0.03) in S-HDL-treated animals compared to controls.

Taken together, these data demonstrate that just 2 weeks of S-HDL nanoimmunotherapy had rapid effects on different atherosclerosis-related parameters with no measurable toxicity.

Discussion

A record 1,500+ nanomedicine-related studies were published in 2018, according to the Web of Science. However, until late 2017, only 50 nanodrugs were available for clinical use in the United States (12). When nanoformulations reach late clinical trial phases, the vast majority of them fail to show their purported advantages over the free drug and hence any additional benefit to patients. This abysmal gap between preclinical nanomedicine and clinical application reflects the numerous translational challenges facing the field. While many factors likely contribute to this gap, oftentimes translation fails because of a lack of appropriate evaluation before moving to humans. In this study, we show the translational workflow we developed to escalate a nanoimmunotherapy's evaluation from mouse to large rabbit and porcine atherosclerosis models.

In our quest to translate our S-HDL nanoimmunotherapy, we first faced the need to produce bulk amounts of nanoimmunotherapeutic to treat large animals. We handled this issue by developing and implementing a new scaled-up microfluidizer-based method that affords an 80-fold higher production rate. Notably, the resulting material had similar physicochemical properties to the traditionally produced nanoimmunotherapy. Most importantly, the scaled-up nanoimmunotherapeutic's *in vivo* behavior, including its biodistribution, pharmacokinetic profile, ability to reach the plaque and therapeutic efficacy, were comparable to our previous observations with benchtop-produced S-HDL.

Non-invasive imaging can probe molecular processes *in vivo* and is therefore a very powerful tool for evaluating new therapies. In fact, imaging is increasingly integrated in clinical trials to provide surrogate endpoints of treatment response without the need for long follow-up periods or large patient cohorts (13). In this study, we used imaging at two different stages in the translational workflow. First, we conducted a quantitative *in vivo*

performance evaluation using a radiolabeled analog of the nanoimmunotherapy, which allowed us to verify plaque accumulation and visualize overall biodistribution. Second, we developed a multiparametric imaging protocol to quantify the effect of nanoimmunotherapy on several disease markers. The complexity of the atherosclerotic process mandates the use of a multimodal approach, allowing assessment of plaque morphology and activity to better characterize lesions. PET/MRI is very well suited to this task, as it combines MRI's excellent soft tissue contrast and spatial resolution with PET's high sensitivity and the specificity of the radiotracers. Despite the treatment's short duration, our results show a clear trend towards reduction in all evaluated atherosclerosis burden parameters, including vessel wall thickness and permeability, inflammation and proliferation. This latter outcome seems to mirror our observations from previous studies, since S-HDL nanoimmunotherapy exerts its effects through macrophage proliferation inhibition (7), which is a dominant process in plaque inflammation in advanced atherosclerosis.

The use of HDL nanobiologics as myeloid cell-specific therapies is a promising treatment avenue for many immune-related diseases. One of the biggest hurdles for clinically translating these nanoimmunotherapies will be implementing large-scale APOA1 extraction/production methods. In this study, we optimized a high throughput method to isolate APOA1 through purification and delipidation of human HDL. While this is a convenient way to extract the protein, safety concerns regarding sterility and risk of contamination would need to be addressed. Alternatively, APOA1 can be produced recombinantly in bacteria or mammalian cells, but production and purification processes in this case can be troublesome and result in low yields.

Another pivotal issue in developing and translating these nanoimmunotherapies is assessing their safety. Simvastatin can have deleterious effects on muscle and liver, especially with higher doses. Yet our nanoimmunotherapy's uptake in muscle was low. Blood biochemistry analysis revealed no difference in creatine phosphokinase, indicating our treatment had no harmful effect on myocytes. In contrast to muscle tissue, our nanoimmunotherapy is taken up by the liver in high quantities, as shown by the biodistribution data. Therefore, it is vital to evaluate signs of liver toxicity. In previous mouse studies, we observed neither metabolic changes nor signs of liver toxicity (14). Our current study confirms this point as transaminases (ALT and AST), alkaline phosphatase and bilirubin levels were unaffected. Effects on the immune system must also be investigated. We observed no changes in white blood cell count, or in lymphocyte, neutrophil and monocyte numbers.

The promising results we obtained in large animals are encouraging and may represent a new therapeutic option for acutely treating atherosclerosis-related inflammation. This option has clinically relevant value after an acute cardiovascular event, *i.e.* myocardial infarction or stroke. These events are known to exacerbate inflammation and thus aggravate ongoing atherosclerosis, leading to a high recurrence rate of acute events in these patients. Thus, it is conceivable that an intervention with our nanoimmunotherapy after a cardiovascular event may be beneficial by rapidly suppressing the exaggerated inflammatory activity in atherosclerotic lesions during that critical period (15).

Our study has limitations. First, owing to logistical considerations, the number of large animals was limited. A total of six pigs were used to develop the imaging protocols, plus another 12 for the biodistribution and efficacy studies. For symmetry, we used the same number of rabbits. However, implementing a longitudinal multiparametric imaging-based therapy monitoring approach allowed us to measure treatment response in individual animals from different angles, *i.e.* assessing different markers of disease progression. Second, using FDG as an imaging marker of inflammation may also have certain limitations in large plaques, since hypoxia-induced uptake may be predominant (16). This could have masked the anti-inflammatory effects of S-HDL to a certain degree.

In conclusion, we presented the production scaling and imaging-facilitated development workflow for evaluating a nanoimmunotherapeutic. In the context of cardiovascular disease, we showed that our nanoimmunotherapeutic's anti-atherosclerotic effects in mice were maintained in large animals. Not only do we anticipate increased potential for nanomedicines as immunotherapeutics, we also demonstrate the value of – and need for – non-invasive imaging readouts when evaluating such nanoimmunotherapies in large animal disease models.

Materials and Methods

Materials

Phospholipids (DMPC, MHPC and DSPE) and simvastatin were purchased from Avanti Polar Lipids (Alabaster, AL) and AK Scientific (Union City, CA), respectively. All other chemicals were acquired from Sigma-Aldrich (St. Louis, MO). APOA1 was isolated from human HDL concentrates (Bioresource Technology, Weston, FL) following a previously described procedure (17). ^{89}Zr was produced at Memorial Sloan-Kettering Cancer Center on an EBCO TR19/9 variable-beam energy cyclotron (Ebco Industries Inc., Vancouver, BC, Canada) via the ^{89}Y(p,n)^{89}Zr reaction and purified in accordance with previously reported methods(18). ^{18}F was produced via the^{18}O(p,n)^{18}F reaction using a GEMS PETtrace-800 cyclotron (GE Healthcare, Chicago, IL).

Radiotracers

^{18}F-labeled 2-deoxy-2-fluoro-D-glucose (^{18}F-FDG) was purchased from NCM USA (Bronx, NY), while ^{18}F-labeled 3'-fluoro-3'-deoxythymidine (^{18}F-FLT) was synthesized in-house by adapting already published procedures (19, 20). Briefly, a QMA cartridge containing cyclotron-produced [^{18}F]fluoride was eluted with a solution containing 9 mg 4,7,13,16,21,24-hexaoxa-1,10 diazabicyclo[8.8.8]hexacosane (Kryptofix [2.2.2]), 0.08 mL 0.15 M K_2CO_3 and 1.92 mL acetonitrile into a 5 mL reaction vial. Solvents were removed azeotropically at 120 °C under a slight flow of nitrogen. Then, 5 mg of precursor 3-*N*-Boc-5'-*O*-dimethoxytrityl-3'-*O*-nosyl-thymidine (ABX, Dresden, Germany) (6.02 μmol) in 500 μL dry acetonitrile was added and the reaction mixture was heated to 150 °C for 10 min. After cooling to room temperature, 1 N hydrochloric acid (400 μL) was added and the mixture was heated to 90 °C for 10 min. The reaction mixture was finally quenched by adding 2 M sodium acetate solution (1.3 mL) and purified by HPLC to yield pure ^{18}F-FLT using a C-18 semi-preparative column (Luna C-18, 250 × 10 mm, 5μm; Phenomenex,

Torrance, CA) and isocratic elution with 8% EtOH/92% water at 5.5 mL*min^{-1} flow (RT ~ 16 min). Purity was assessed via Radio-HPLC using a C-18 analytical column (Atlantis T3, 100Å, 250 × 4.6 mm, 5μm; Waters, Milford, MA) and isocratic elution with 10% EtOH/90% water at 1mL* min^{-1} flow (RT = 7.4 min).

HPLC and Radio-HPLC

HPLC was performed on a Prominence HPLC system (Shimadzu, Kyoto, Japan) equipped with two LC-10AT pumps and an SPD-M10AVP photodiode array detector. Radio-HPLC was performed using a Lablogic Scan-RAM Radio-TLC/HPLC detector. Size exclusion chromatography was performed on a Superdex 10/300 column (GE Healthcare Life Sciences, Pittsburgh, PA) using PBS as eluent at a flow rate of 1 mL/min.

Animals

Female *Apoe*$^{-/-}$ mice were purchased from Jackson Laboratories (Sacramento, CA). Male CRL SPF White New Zealand rabbits (n=12) and male familial hypercholesterolemia pigs (n=11; 4 males and 7 females) were acquired from Charles River Laboratories (Wilmington, MA) and University of Wisconsin, respectively. All animal experiments were performed in accordance with protocols approved by the Institutional Animal Care and Use Committees of Mount Sinai, Memorial Sloan Kettering Cancer Center and/or Skirball Center for Cardiovascular Research and followed National Institutes of Health guidelines for animal welfare.

Mouse model of atherosclerosis

Female *Apoe*$^{-/-}$ mice (B6.129P2-Apoe$^{tm1Unc/J}$, 4–6 weeks old) were fed a high-fat diet (Harlan Teklad TD.88137, 42% calories from fat; Envigo, Somerset, NJ) for 12 weeks. Under these conditions, this animal model develops atherosclerotic lesions due to high LDL cholesterol concentrations in blood resulting from their lack of apolipoprotein E (21, 22).

Rabbit model of atherosclerosis (23, 24)

Male CRL SPF White New Zealand rabbits (2.5–3 months old) underwent double balloon injury of the thoracic and abdominal aorta to induce atherosclerosis. Denudation was performed by introducing a 4F-Fogarty embolectomy catheter (Edwards Lifesciences, Irvine, CA) through the femoral artery and inflating the balloon to 2 atm under fluoroscopic guidance. The procedure was repeated on the contralateral extremity 4 weeks later. Surgery was performed under anesthesia with intramuscular ketamine (35 mg/kg) and xylazine (5 mg/kg). To further accelerate plaque progression, animals were fed a high-cholesterol diet (Research Diets, New Brunswick, NJ) enriched initially with 0.3% cholesterol for 8 weeks and subsequently 0.15% for at least 8 weeks.

Porcine model of atherosclerosis (25)

We used the familial hypercholesterolemia swine (FHS) model of atherosclerosis. Due to a mutation in Lpb5 at the apolipoprotein B locus, these animals carry a liver low-density lipoprotein receptor deficiency that results in hypercholesterolemia and atherosclerosis. To accelerate plaque development, animals were fed a high-fat diet (enriched with 2%

cholesterol) for 12 weeks and balloon injuries were performed in the deep and superficial femoral arteries on both legs with access through the carotid artery with a 4F-Fogarty embolectomy catheter (Edwards Lifesciences, Irvine, CA).

Synthesis of S-HDL by high-pressure microfluidic homogenization

Simvastatin and phospholipids 1-myristoyl-2-hydroxy-*sn*-glycero-phosphocholine (MHPC) and 1,2-dimyristoyl-*sn*-glycero-3-phosphatidylcholine (DMPC) were mixed in chloroform/methanol 4:1 in a 2-liter round bottom flask. A lipid film was formed by reduced-pressure rotary evaporation removal of solvents. The resulting film was further dried under a nitrogen flow for 1 hour. A solution of APOA1 was added, followed by PBS to reach a volume of approximately 0.5 L. The film was left to hydrate at 37 °C using a rotary evaporator to facilitate mixing. In batches of 0.25 L, the crude suspension underwent high-pressure microfluidics homogenization using a microfluidizer 110-S (Microfluidics, Newton, MA). The solution was pressurized at 120 psi to pass through the microfluidics chamber, which was refrigerated with an ice/water bath, 8 to 12 times. The resulting solution was left overnight at room temperature and then centrifuged at 4,000 rpm for 1 hour at 4 °C. The supernatant was then passed through a 0.2 μm Stericup Vacuum Filter Unit (MilliporeSigma, Burlington, MA), and subsequently concentrated and washed twice with PBS using a 100 kDa Vivaflow device (Sartorius, Göttingen, Germany). After the final concentration round, the final volume was ~0.1 L. Samples were left overnight at 4 °C and then centrifuged at 4,000 rpm for 1 hour at 4 °C. Finally, the supernatant was passed through a 0.2 μm Stericup Vacuum Filter Unit (MilliporeSigma, Burlington, MA) under clean, sterile conditions and kept at 4 °C until use. Due to simvastatin's sensitivity to light, samples were protected from light during the whole formulation process.

S-HDL quality control

Size, dispersity and simvastatin concentration were measured for every S-HDL batch to assess the production quality. Size and dispersity were determined just after homogenization and at the end of the purification/sterilization process by dynamic light scattering, using a Zeta PALS analyzer (Brookhaven Instruments Corporation, Holtsville, MY). Simvastatin concentration was measured by HPLC using a previously described method (26). Briefly, an aliquot of S-HDL (100 μL) formulation was dried for 18 hours in a desiccator then solubilized in acetonitrile (1 mL) and sonicated for 30 min on ice. After centrifugation (14,000 *g* for 10 min), supernatants were analyzed by reverse phase HPLC using an Ascentis C18 column (100 mm x 4.6 mm, 3 μm particles) using acetonitrile/water 80:20 as eluent. Simvastatin absorption was quantified at 238 nm.

Evaluation of S-HDL treatment efficacy in mice

Female *Apoe*$^{-/-}$ (n=24, 12 weeks on Western diet; weight: 29.6 ± 4.1 g) were randomized into two groups of 12 animals: 1) PBS and 2) S-HDL, at a simvastatin dose of 60 mg/kg body weight. Nanobiologic doses as well as PBS were administered via a lateral tail vein. Treatment consisted of four administrations, one every 48 hours. Twenty-four hours after the last dose, animals were euthanized and extensively perfused with saline, and the aortas were carefully excised for *ex vivo* evaluation by flow cytometry (n=10) and histological analysis (n=2).

Flow cytometry

The aorta, from aortic root to the iliac bifurcation, was gently cleaned of fat, collected and then digested using an enzymatic digestion solution containing liberase TH (4 U/mL) (Roche, Basel, Switzerland), deoxyribonuclease (DNase) I (40 U/mL) (Sigma-Aldrich), and hyaluronidase (60 U/mL) (Sigma-Aldrich, St. Louis, MO) in PBS at 37 °C for 60 minutes. Cells were filtered through a 70 μm cell strainer and washed with serum containing media. Single cell suspensions were stained with the following monoclonal antibodies: anti-CD11b (clone M1/70), anti-F4/80 (clone BM8), anti-CD11c (clone N418), anti-CD45 (clone 30-F11), anti-Ly6C (clone AL-21) and a lineage cocktail (Lin) containing anti-CD90.2 (clone 53–2.1), anti-Ter119 (clone TER119), anti-NK1.1 (clone PK136), anti-CD49b (clone DX5), anti-CD45R (clone RA3–6B2) and anti-Ly6G (clone 1A8). Macrophages were identified as $CD45^{+}$, $CD11b^{hi}$, $Lin^{-/lo}$, $CD11c^{lo}$ and $F4/80^{hi}$. $Ly6C^{hi}$ monocytes were identified as $CD45^{+}$, $CD11b^{hi}$, $Lin^{-/lo}$, $CD11c^{lo}$ and $Ly6C^{hi}$. Data were acquired on an LSRII flow cytometer (BD Biosciences, Woburn, MA), and the data were analyzed using FlowJo v10.0.7 (Tree Star, Ashland, OR).

Antibody	Vendor	Catalog number
Anti-mouse CD11b (clone M1/70)	BioLegend	101228
Anti-mouse F4/80 (clone BM8)	BioLegend	123114
Anti-mouse CD11c (clone N418)	BioLegend	117310
Anti-mouse CD45 (clone 30-F11)	BioLegend	103138
Anti-mouse Ly6C (clone AL-21)	BD Biosciences	560592
Anti-mouse CD90.2 (clone 53–2.1)	eBioScience	48–0902–82
Anti-mouse Ter119 (clone TER119)	eBioScience	48–5921–82
Anti-mouse NK1.1 (clone PK136)	eBioScience	48–5941–82
Anti-mouse CD49b (clone DX5)	eBioScience	48–5971–82
Anti-mouse CD45R/B220 (clone RA3–6B2)	eBioScience	48–0452–82
Anti-mouse Ly6G (clone 1A8)	BioLegend	127612

Radiolabeling of S-HDL

Ready-to-label S-HDL was prepared following a previously described procedure (9) by adding 0.7 weight % of the phospholipid chelator DSPE-DFO (27) to the lipid mix at the expense of DMPC. The resulting nanoparticles were radiolabeled following a previously reported method (9). Briefly, DFO-bearing S-HDL was reacted with ^{89}Zr-oxalate at a ratio of ~37 MBq/mg APOA1 in phosphate buffered saline (PBS, pH = 6.8–7.1) at 37 °C for 2 hours. [^{89}Zr]-S-HDL was purified by centrifugal filtration using 10 kDa molecular weight cut-off Visvaspin tubes. Radiochemically pure [^{89}Zr]-S-HDL was mixed with unlabeled S-HDL to achieve the desired simvastatin dose, and the mixture was allowed to equilibrate for at least 4 hours.

Fluorescent labeling of S-HDL

For NIRF imaging, DiD-S-HDL was prepared, as previously reported (6, 7), by adding DiD to the phopholipid/simvastatin mix at a 1.5% w/w during the lipid film formation process.

Finally, DiD-S-HDL was mixed with unlabeled S-HDL to achieve the desired simvastatin dose.

PET/CT imaging, biodistribution and pharmacokinetics in mice

Apoe$^{-/-}$ mice (n=4; 12 weeks on high-fat diet) were injected with [^{89}Zr]-S-HDL (7.0 ± 1.1 MBq, 60 mg simvastatin/kg) in 150–200 μL PBS solution via the lateral tail vein. At 2 and 30 min and 2, 6 and 18 hours, blood (5–10 μL) was sampled from the tail vein and weighed. Radioactivity content was measured using a Wizard^2 2480 automatic gamma counter (Perkin Elmer, Waltham, MA). At 24 hours post administration, animals were anesthetized with isoflurane (Baxter Healthcare, Deerfield, IL)/oxygen gas mixture (2% for induction, 1 % for maintenance), and a scan was then performed using an Inveon PET/CT scanner (Siemens Healthcare Global, Erlangen, Germany). Whole body PET static scans recording a minimum of 30 million coincident events were performed, with duration of approximately 20 min. The energy and coincidence timing windows were 350−700 keV and 6 ns, respectively. The image data were normalized to correct for non-uniform PET response, dead-time count losses, positron branching ratio and physical decay to the time of injection, but no attenuation, scatter or partial-volume averaging correction was applied. Whole body standard low magnification CT scans were performed with the following acquisition parameters: voltage of 80 kV, current of 500 μA, exposure time of 145 ms per frame and 120 rotational steps for a total of 220 degrees.

After the scan, at 26 h p.i., animals were euthanized and perfused with PBS. Tissues of interest (blood, kidneys, liver, spleen, lungs, heart, brain, aorta and muscle) were collected, blotted and weighed before radioactivity counting on a Wizard^2 2480 automatic gamma counter. Radioactivity values were corrected for decay and normalized to tissue weight to express radioactivity concentration as percentage injected dose per gram (%ID/g).

[^{89}Zr]-S-HDL PET imaging, biodistribution and plaque targeting in rabbits and pigs

[^{89}Zr]-S-HDL was administered via the ear vein to atherosclerotic rabbits (n=2, 20.4 ± 3.1 MBq, 15 mg simvastatin/kg) and pigs (n=2, 142.4 ± 18.3 MBq, 7.5 mg simvastatin/kg) while anesthetized on the bed of a Siemens Biograph mCT PET/CT time-of-flight (TOF) scanner. For the CT scan, iodine contrast (Iopamidol injection 76%, Bracco Diagnostics, Monroe Township, NJ) was injected in rabbits (10 mL, 1 mL/s, no delay) and pigs (70 mL, 1 mL/s, 6 s delay). Whole-body static scans were acquired 0.5, 24 and 48 hours post injection. Before PET acquisition, a CT scan was recorded with the following parameters: voltage, 140 kVp; tube current, 34 mA; exposure time, 1000 ms; slice thickness, 1 mm. The CT scan was used for attenuation correction of the PET data.

In addition to biodistribution imaging by PET/CT, the ability of the nanoimmunotherapeutic to reach and accumulate in atherosclerotic plaques was imaged *in vivo* using PET/MRI. After the 48-hour PET/CT scan, animals were transferred to a Siemens Biograph mMR 3T PET/MRI scanner and imaged using a body matrix coil. After scout scans, a bright-blood, 3D time-of-flight (TOF) non-contrast enhanced angiography sequence was acquired to better localize arterial anatomical landmarks (rabbits: renal arteries and iliac bifurcation, pigs: superficial femoral arteries). Imaging parameters for the rabbit protocol were: TR, 23 ms;

TE, 2.83 ms; flip angle 20 degrees; spatial resolution, 0.7×0.7×1 mm^3; acquisition plane, axial; number of slices, 200; number of signal averages, 1, and the parameters for the pig protocol were: TR, 23 ms; TE, 3.69 ms; flip angle 20 degrees; spatial resolution, 1.4×1.4×1.5 mm^3; acquisition plane, axial; number of slices, 228; number of signal averages, 1. Subsequently, the PET scan was initiated simultaneously with a black-blood, 3D T2-weighted SPACE (Sampling Perfection with Application optimized Contrasts using different flip angle Evolution) sequence acquired for vessel wall delineation, with the following imaging parameters for rabbits: TR, 1600 ms; TE, 115 ms; spatial resolution, 0.63×0.63×0.63 mm^3; acquisition plane, sagittal; number of slices, 30; number of signal averages, 4, and the parameters for pigs were: TR, 1200 ms; TE, 112 ms; spatial resolution, 0.63×0.63×0.63 mm^3; acquisition plane, coronal; number of slices, 144; number of signal averages, 4. Attenuation correction of PET images was performed using the built-in MR-based attenuation correction (MR-AC) map, obtained from a two-point Dixon sequence allowing for fat/water separation. Rabbit attenuation maps were segmented into 2 compartments (soft tissue and air), while pigs attenuation maps were segmented into 4 compartments (soft tissue, fat, air and lungs). Shortly after the last scan, animals were euthanized, rabbits were thoroughly perfused with isotonic saline and tissues of interest (liver, spleen, kidney, lung, muscle and artery of interest) were collected for *ex vivo* radioactivity quantification, as described above, near-infrared fluorescence imaging and autoradiography. In both cases, PET images were reconstructed using the ordinary Poisson Ordered subset expectation–maximization (OP-OSEM) algorithm with point-spread function correction. Image analysis was conducted using OsiriX Imaging Software by drawing regions of interest (ROIs) on the selected tissues (liver, kidneys, spleen for both rabbit and pigs, as well as abdominal aorta – from renal artery to iliac bifurcation – and superficial femoral arteries for rabbit and pigs, respectively). Blood activity was quantified in the left ventricle. Standardized uptake values (SUVs, defined as [Pixel value (Bq/mL) * Weight of the subject (kg) / Dose (Bq)] * 1000 g/kg) were obtained by averaging SUV_{mean} or SUV_{max} values in each ROI drawn on at least five slices of the organ of interest and on all slices of the abdominal aorta (rabbits) and superficial femoral arteries (pigs). Maximal target-to-background (TBR_{max}) values were calculated by dividing average SUV_{max} from the abdominal aorta (rabbits) and superficial femoral arteries (pigs) by average SUV_{max} from muscle in the same animal.

Evaluation of S-HDL treatment efficacy in rabbits and pigs

Rabbits (n=10, weight 3.5 ± 0.3 kg) and pigs (n=8, weight 31.2 ± 5.7 kg) with atherosclerosis were randomized into two groups of five animals, receiving either PBS or S-HDL. The simvastatin dose was 15 and 7.5 mg/kg for rabbits and pigs, respectively. Treatment consisted of four intravenous injections, one every 4 days. Response was evaluated non-invasively and longitudinally using a multiparametric PET/MR imaging protocol (see below). Shortly after the last scan and 30 min prior to euthanasia, Evans blue was injected i.v. for *ex vivo* assessment of vessel wall permeability. Immediately following euthanasia animals were perfused with isotonic saline and tissues of interest (aorta for rabbits, femoral tree for pigs) were collected for *ex vivo* evaluation by near-infrared fluorescence imaging and histological analysis. The femoral tree was thoroughly rinsed in isotonic saline once harvested.

Non-invasive PET/MR imaging evaluation of S-HDL treatment response in rabbits and pigs

A multiparametric PET/MR imaging protocol was implemented to monitor treatment. Twenty-four hours before the first injection, animals underwent a PET/MR imaging session consisting of ^{18}F-FDG-based assessment of plaque inflammation and 3D anatomical MRI using the 3D T2-weighted SPACE sequence described above. The next day, animals had a second PET/MR imaging session to determine plaque macrophage proliferation with ^{18}F-FLT and vessel wall permeability by 3D dynamic contrast-enhanced (DCE) MRI. DCE-MRI was performed using a 3D motion-sensitized driven equilibrium prepared rapid gradient echo (MERGE) sequence to simultaneously achieve blood pool signal suppression, and signal enhancement in atherosclerotic plaques. 3D DCE-MRI parameters in rabbits were: TR, 491.08 ms; TE, 5.32 ms; flip angle 20 degrees; spatial resolution, 0.63×0.63×0.63 mm^3; acquisition plane, sagittal; number of slices, 20; number of dynamics, 20; number of signal averages, 1; temporal resolution, 31 s, and the parameters for pigs were: TR, 1106.1 ms; TE, 4.3 ms; flip angle 20 degrees; spatial resolution, 0.63×0.63×0.63 mm^3; acquisition plane, coronal; number of slices, 40; number of dynamics, 12; number of signal averages, 1; temporal resolution, 101 s. Dynamic images were acquired before, during and after the injection of 0.2 mmol/Kg of Gd-DTPA (Magnevist, Bayer). The same imaging sessions were performed at the end of treatment, on days 14 and 15 after the first injection. Radiotracers ^{18}F-FDG ($rabbits_{baseline}$: 118.4 ± 17.4 MBq, n=10; $rabbits_{terminal}$: 121.4 ± 16.4 MBq, n=10), ($pigs_{baseline}$: 260.3 ± 14.7 MBq, n=10; $pigs_{terminal}$: 269.5 ± 32.8 MBq, n=10) and ^{18}F-FLT ($rabbits_{baseline}$: 108.8 ± 24.5 MBq, n=10; $rabbits_{terminal}$: 119.4 ± 12.2 MBq, n=10) and ($pigs_{baseline}$: 230.2 ± 34.0 MBq, n=10; $pigs_{terminal}$: 201.7 ± 54.1 MBq, n=10) were administered via the ear vein. For ^{18}F-FDG imaging, animals were fasted for at least 6 hours before the scan, which was performed 2.5 hours (rabbits) and 1 hour (pigs) after administration. ^{18}F-FLT PET scans were performed 2 hours (rabbits) and 1 hour (pigs) post injection with acquisition times of 30 min for each tracer. Both PET imaging sessions were performed on a Siemens mMR 3T PET/MRI scanner using a body matrix coil.

Near-infrared fluorescence imaging

Shortly after euthanasia, perfused tissue samples were placed on thick black paper and imaged on a Xenogen IVIS Spectrum Preclinical Imaging System (Perkin Elmer, Waltham, MA). Fluorescence images were acquired with selected excitation and emission band-pass filters: DiD (λ_{Exc} = 640 nm, λ_{Em} = 680 nm) and Evans Blue (λ_{Exc} = 605, λ_{Em} = 680 nm). Exposure time for each image was 4 s. Data were processed and analyzed using Living Image software (Perkin Elmer) by drawing a region of interest around the arteries of interest and quantified as radiant efficiency.

Autoradiography

Following euthanasia, animals were perfused and their aortas (mice and rabbits) or femoral arteries (pigs) were excised and blotted. To determine radiotracer distribution, digital autoradiography was performed by placing tissue samples in a film cassette against a phosphorimaging plate (BASMS-2325, Fujifilm, Valhalla, NY) for 2 hours (mouse aortas) or 48 hours (rabbit aortas, pig femoral arteries) at −20 °C. Phosphorimaging plates were read at

a pixel resolution of 25 μm with a Typhoon 7000IP plate reader (GE Healthcare, Pittsburgh, PA). Quantification was carried out using ImageJ software.

Histology and immunohistochemistry

Tissue samples from mice, rabbits and pigs were placed in paraformaldehyde overnight and subsequently embedded in paraffin. Sections were taken from the aortic arch in mice, from the abdominal aorta of rabbits, and from the abdominal aorta just proximal to the iliac bifurcation and from the largest palpable plaque in the right femoral artery in pigs. Samples were cut in 5-μm sections, mounted on slides and stained with Hematoxylin & Eosin (rabbits), Masson trichrome (mice, rabbits and pigs), CD68 (mice) and RAM-11(rabbits) according to standard protocols.

Blood tests in pigs

Blood was collected by vena puncture from all pigs at the end of the study. Serum was sent to IDEXX Laboratories (Totowa, NJ) and analyzed using an Olympus AU400 Chemistry Analyzer. Whole blood was collected in EDTA-containing tubes and analyzed using an IDEXX procyte DX Hematology Analyzer for complete blood count analysis.

Statistics

Data are presented as mean ± SD, unless otherwise stated. Mann-Whitney tests were used to assess group differences. In the therapeutic study in rabbits and pigs, a linear mixed model (LMM) was used to statistically analyze differences in imaging-derived parameters between treatment groups. The imaging parameter at the end of the study (terminal scan) was used as the dependent variable. Type of treatment and imaging parameter at the start of the study (baseline) were defined as fixed effects, and the side (left or right femoral artery in pigs) as a random effect. For all tests, $\alpha < 0.05$ represents statistical significance. Statistical analyses were performed with GraphPad Prism®, Version 6.0c (La Jolla, CA).

Supplementary Material

Refer to Web version on PubMed Central for supplementary material.

Acknowledgments

Funding: This work was supported by the National Institutes of Health grants R01 EB009638, P01 HL131478 (Z.A.F.); R01 HL125703, R01 HL118440 (W.J.M.M.); P30 CA008748; the American Heart Association 16SDG31390007 (C.P.M.); the Netherlands Organization for Scientific Research NWO Vidi (W.J.M.M) and ZonMW Veni 016156059 (R.D.); the Danish Council for Independent Research DFF-1333-00235A (T.B.); the Danish Cancer Society R71-A4285 (T.B.); and the Rigshospitalets Research Foundation (T.B.). The authors also thank the Center for Molecular Imaging and Nanotechnology (CMINT) for financial support (T.R.).

References and Notes

1. Wilhelm S, Tavares AJ, Dai Q, Ohta S, Audet J, Dvorak HF, Chan WCW, Analysis of nanoparticle delivery to tumours, Nat. Rev. Mater 1, 16014 (2016).
2. Lameijer M, Binderup T, van Leent MMT, Senders ML, Fay F, Malkus J, Sanchez-Gaytan BL, Teunissen AJP, Karakatsanis N, Robson P, Zhou X, Ye Y, Wojtkiewicz G, Tang J, Seijkens TTP, Kroon J, Stroes ESG, Kjaer A, Ochando J, Reiner T, Pérez-Medina C, Calcagno C, Fischer EA, Zhang B, Temel RE, Swirski FK, Nahrendorf M, Fayad ZA, Lutgens E, Mulder WJM,

Duivenvoorden R, Efficacy and safety assessment of a TRAF6-targeted nanoimmunotherapy in atherosclerotic mice and non-human primates, Nat. Biomed. Eng 2, 279–292 (2018). [PubMed: 30936448]

3. Duivenvoorden R, Senders ML, van Leent MMT, Pérez-Medina C, Nahrendorf M, Fayad ZA, Mulder WJM, Nanoimmunotherapy to treat ischaemic heart disease, Nat. Rev. Cardiol 16, 21–32 (2019). [PubMed: 30209355]
4. Braza MS, van Leent MMT, Lameijer M, Sanchez-Gaytan BL, Arts RJW, Pérez-Medina C, Conde P, Garcia MR, Gonzalez-Perez M, Brahmachary M, Fay F, Kluza E, Kossatz S, Dress RJ, Salem F, Rialdi A, Reiner T, Boros P, Strijkers GJ, Calcagno CC, Ginhoux F, Marazzi I, Lutgens E, Nicolaes GAF, Weber C, Swirski FK, Nahrendorf M, Fisher EA, Duivenvoorden R, Fayad ZA, Netea MG, Mulder WJM, Ochando J, Inhibiting Inflammation with Myeloid Cell-Specific Nanobiologics Promotes Organ Transplant Acceptance, Immunity 49, 819–828.e6 (2018). [PubMed: 30413362]
5. Bird L, Targeting trained immunity, Nat. Rev. Immunol 19, 2–3 (2018).
6. Duivenvoorden R, Tang J, Cormode DP, Mieszawska AJ, Izquierdo-Garcia D, Ozcan C, Otten MJ, Zaidi N, Lobatto ME, van Rijs SM, Priem B, Kuan EL, Martel C, Hewing B, Sager H, Nahrendorf M, Randolph GJ, Stroes ESG, Fuster V, a Fisher E, a Fayad Z, Mulder WJM, A statin-loaded reconstituted high-density lipoprotein nanoparticle inhibits atherosclerotic plaque inflammation., Nat. Commun 5, 3065 (2014). [PubMed: 24445279]
7. Tang J, Lobatto ME, Hassing L, van der Staay S, van Rijs SM, Calcagno C, Braza MS, Baxter S, Fay F, Sanchez-Gaytan BL, Duivenvoorden R, Sager HB, Astudillo YM, Leong W, Ramachandran S, Storm G, Pérez-Medina C, Reiner T, Cormode DP, Strijkers GJ, Stroes ESG, Swirski FK, Nahrendorf M, Fisher EA, Fayad ZA, Mulder WJM, Inhibiting macrophage proliferation suppresses atherosclerotic plaque inflammation, Sci. Adv 1 (2015).
8. Sanhai WR, Sakamoto JH, Canady R, Ferrari M, Seven challenges for nanomedicine, Nat. Nanotechnol 3, 242–244 (2008). [PubMed: 18654511]
9. Pérez-Medina C, Tang J, Abdel-Atti D, Hogstad B, Merad M, Fisher EA, Fayad ZA, Lewis JS, Mulder WJM, Reiner T, PET imaging of tumor-associated macrophages with 89Zr-labeled high-density lipoprotein nanoparticles, J. Nucl. Med 56, 1272–1277 (2015). [PubMed: 26112022]
10. https://www.fda.gov/downloads/Drugs/Guidances/UCM078932.pdf
11. Pérez-Medina C, Binderup T, Lobatto ME, Tang J, Calcagno C, Giesen L, Wessel CH, Witjes J, Ishino S, Baxter S, Zhao Y, Ramachandran S, Eldib M, Sánchez-Gaytán BL, Robson PM, Bini J, Granada JF, Fish KM, Stroes ESG, Duivenvoorden R, Tsimikas S, Lewis JS, Reiner T, Fuster V, Kjær A, Fisher EA, Fayad ZA, Mulder WJM, In Vivo PET Imaging of HDL in Multiple Atherosclerosis Models, JACC Cardiovasc. Imaging 9, 950–961 (2016). [PubMed: 27236528]
12. Ventola CL, Progress in Nanomedicine: Approved and Investigational Nanodrugs., P T 42, 742–755 (2017). [PubMed: 29234213]
13. Fayad ZA, Mani V, Woodward M, Kallend D, Abt M, Burgess T, Fuster V, Ballantyne CM, Stein EA, Tardif J-C, Rudd JHF, Farkouh ME, Tawakol A, dal-PLAQUE Investigators, Safety and efficacy of dalcetrapib on atherosclerotic disease using novel non-invasive multimodality imaging (dal-PLAQUE): a randomised clinical trial, Lancet 378, 1547–1559 (2011). [PubMed: 21908036]
14. Alaarg A, Senders ML, Varela-Moreira A, Pérez-Medina C, Zhao Y, Tang J, Fay F, Reiner T, Fayad ZA, Hennink WE, Metselaar JM, Mulder WJM, Storm G, A systematic comparison of clinically viable nanomedicines targeting HMG-CoA reductase in inflammatory atherosclerosis, J. Control. Release 262, 47–57 (2017). [PubMed: 28700897]
15. Ridker PM, Everett BM, Thuren T, MacFadyen JG, Chang WH, Ballantyne C, Fonseca F, Nicolau J, Koenig W, Anker SD, Kastelein JJP, Cornel JH, Pais P, Pella D, Genest J, Cifkova R, Lorenzatti A, Forster T, Kobalava Z, Vida-Simiti L, Flather M, Shimokawa H, Ogawa H, Dellborg M, Rossi PRF, Troquay RPT, Libby P, Glynn RJ, Antiinflammatory Therapy with Canakinumab for Atherosclerotic Disease, N. Engl. J. Med 377, 1119–1131 (2017). [PubMed: 28845751]
16. Folco EJ, Sheikine Y, Rocha VZ, Christen T, Shvartz E, Sukhova GK, Di Carli MF, Libby P, Hypoxia But Not Inflammation Augments Glucose Uptake in Human Macrophages, J. Am. Coll. Cardiol 58, 603–614 (2011). [PubMed: 21798423]
17. Zamanian-Daryoush M, Lindner D, Tallant TC, Wang Z, Buffa J, Klipfell E, Parker Y, Hatala D, Parsons-Wingerter P, Rayman P, Yusufishaq MSS, Fisher EA, Smith JD, Finke J, DiDonato JA,

Hazen SL, The cardioprotective protein apolipoprotein A1 promotes potent anti-tumorigenic effects, J. Biol. Chem 288, 21237–52 (2013). [PubMed: 23720750]

18. Holland JP, Sheh Y, Lewis JS, Standardized methods for the production of high specific-activity zirconium-89., Nucl. Med. Biol 36, 729–39 (2009). [PubMed: 19720285]
19. Kolb HC, Padgett HC, Zigler S, Patanella J, Mu F, Gangadharmath UB, Mocharla VP, Scott PJH, Walsh JC, in Radiochemical Syntheses, (John Wiley & Sons, Inc., Hoboken, NJ, USA, 2012), pp. 21–30.
20. Shao X, Hoareau R, Hockley B, Modification of fluorine-18 synthesis modules to enable cGMP synthesis of radiopharmaceuticals using multiple radiochemical strategies, J. Nucl. Med 51, s2, 1453 (2010)
21. Plump AS, Smith JD, Hayek T, Aalto-Setälä K, Walsh A, Verstuyft JG, Rubin EM, Breslow JL, Severe hypercholesterolemia and atherosclerosis in apolipoprotein E-deficient mice created by homologous recombination in ES cells., Cell 71, 343–53 (1992). [PubMed: 1423598]
22. Nakashima Y, Plump AS, Raines EW, Breslow JL, Ross R, ApoE-deficient mice develop lesions of all phases of atherosclerosis throughout the arterial tree., Arterioscler. Thromb 14, 133–40 (1994). [PubMed: 8274468]
23. Lobatto ME, Calcagno C, Metselaar JM, Storm G, Stroes ESG, Fayad ZA, Mulder WJM, in Methods in enzymology, (2012), vol. 508, pp. 211–228. [PubMed: 22449928]
24. Senders ML, Lobatto ME, Soler R, Lairez O, Pérez-Medina C, Calcagno C, Fayad ZA, Mulder WJM, Fay F, in Methods in molecular biology (Clifton, N.J.), (2018), vol. 1816, pp. 385–400.
25. Granada JF, Milewski K, Zhao H, Stankus JJ, Tellez A, Aboodi MS, Kaluza GL, Krueger CG, Virmani R, Schwartz LB, Nikanorov A, Vascular response to zotarolimus-coated balloons in injured superficial femoral arteries of the familial hypercholesterolemic Swine., Circ. Cardiovasc. Interv 4, 447–55 (2011). [PubMed: 21953371]
26. Kim Y, Fay F, Cormode DP, Sanchez-Gaytan BL, Tang J, Hennessy EJ, Ma M, Moore K, Farokhzad OC, Fisher EA, Mulder WJM, Langer R, Fayad ZA, Single Step Reconstitution of Multifunctional High-Density Lipoprotein-Derived Nanomaterials Using Microfluidics, ACS Nano 7, 9975–9983 (2013). [PubMed: 24079940]
27. Pérez-Medina C, Abdel-Atti D, Zhang Y, Longo VA, Irwin CP, Binderup T, Ruiz-Cabello J, Fayad ZA, Lewis JS, Mulder WJM, Reiner T, A modular labeling strategy for in vivo PET and near-infrared fluorescence imaging of nanoparticle tumor targeting, J. Nucl. Med 55, 1706–1711 (2014). [PubMed: 25060196]

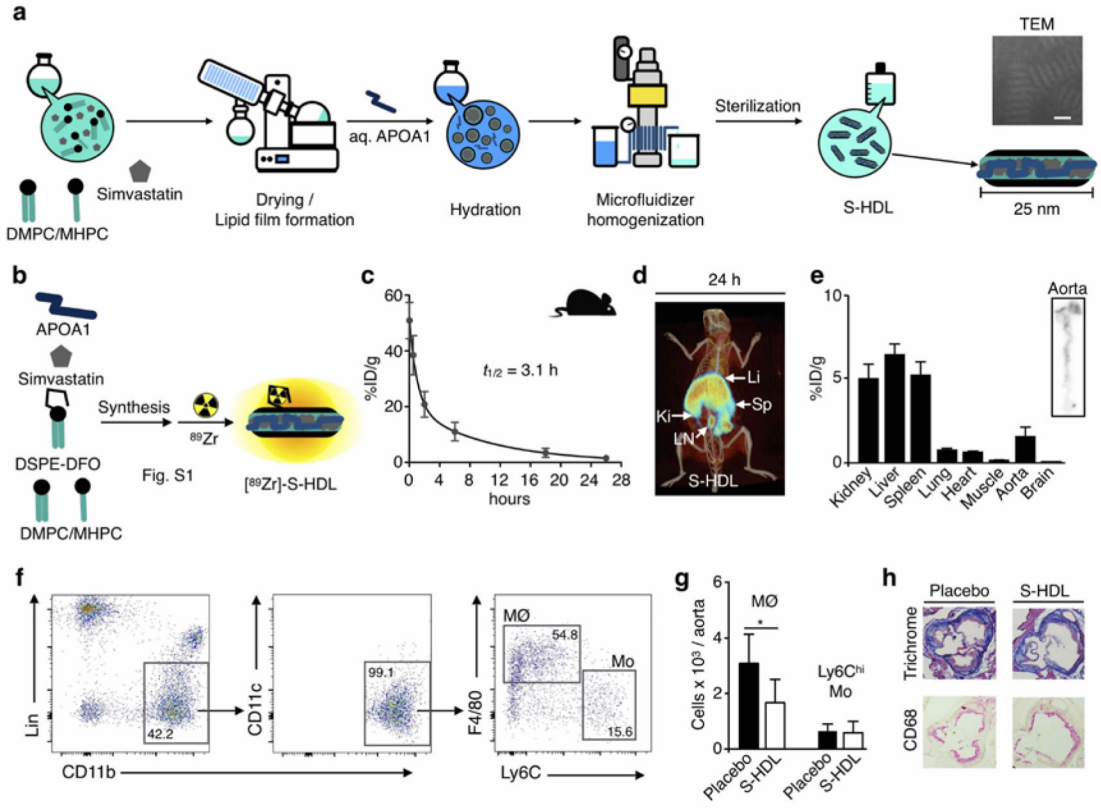

Fig. 1. Nanoimmunotherapy production scale-up and evaluation in *Apoe*$^{-/-}$ mice.

a. Schematic of simvastatin-loaded HDL (S-HDL) production by high-pressure microfluidic homogenization. Scale bar on transmission electron microscopy (TEM) image = 25 nm. **b.** Radiolabeling of S-HDL with ^{89}Zr by incorporating the phospholipid chelator DSPE-DFO in the formulation. **c.** Blood time-activity curve for [^{89}Zr]-S-HDL in *Apoe*$^{-/-}$ mice (n=4, 12 weeks on Western diet). **d.** Representative 3D-rendered PET/CT fusion image of an *Apoe*$^{-/-}$ mouse 26 p.i. of ^{89}Zr-S-HDL. **e.** Tissue radioactivity distribution at 26 hours post injection of [^{89}Zr]-S-HDL in *Apoe*$^{-/-}$ mice (n=4, 12 weeks on Western diet). On the right, representative autoradigraph showing radioactivity distribution on the aorta of an *Apoe*$^{-/-}$ mouse 26 p.i. of ^{89}Zr-S-HDL. **f.** Gating procedure employed in the flow cytometric analysis to evaluate S-HDL treatment efficacy in *Apoe*$^{-/-}$ mice. **g.** Aortic macrophage (MØ) and monocyte (Ly6C^{hi} Mo) numbers after treatment with PBS (Placebo) or S-HDL in *Apoe*$^{-/-}$ mice (n=10 per group, 12 weeks on Western diet). **h.** Representative aortic sections from *Apoe*$^{-/-}$ mice (n=2 per group, 12 weeks on Western diet) treated with PBS (Placebo) or S-HDL. Li = liver; Sp = spleen; Ki = kidney; LN = lymph node. * $P < 0.05$.

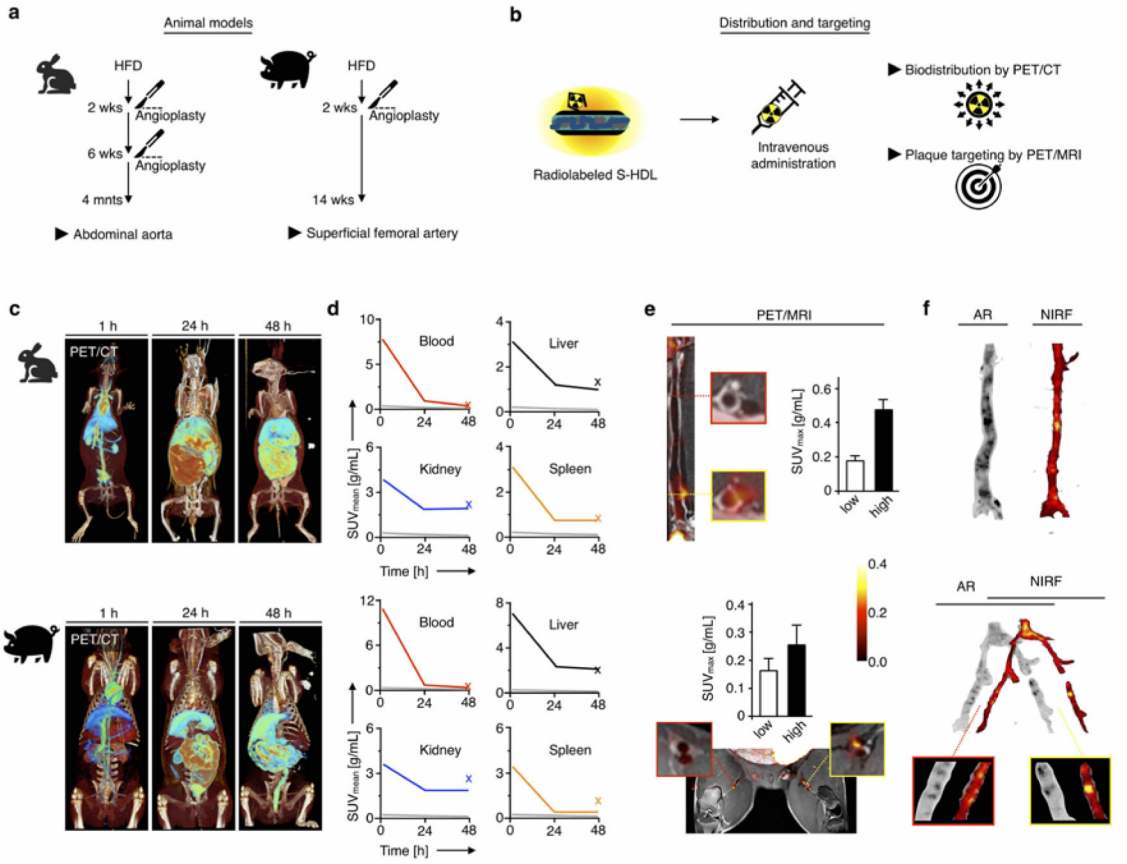

Fig. 2. S-HDL nanoimmunotherapy *in vivo* evaluation by non-invasive imaging in rabbits and pigs.

a. Schematic description of the rabbit and porcine atherosclerosis models used in this study. **b.** ^{89}Zr-S-HDL was used to non-invasively probe biodistribution and plaque targeting by PET/CT and PET/MRI, respectively. **c.** Representative 3D-rendered PET/CT fusion images of atherosclerotic rabbits (top) and pigs (bottom) at 1, 24 and 48 hours post administration of [^{89}Zr]-S-HDL. **d.** PET imaging-derived time-activity curves in selected tissues in rabbits (n=2, top) and pigs (n=2, bottom) injected with [^{89}Zr]-S-HDL. The x represents the value obtained *ex vivo* by gamma counting. The grey line is the muscle time-activity curve, included for reference. **e.** PET/MR imaging assessment of plaque targeting in rabbits (top) and pigs (bottom), 48 hours p.i. of [^{89}Zr]-S-HDL. **f.** Regional distribution of S-HDL in atherosclerotic samples from rabbits (top) and pigs (bottom), as determined by autoradiography (AR, [^{89}Zr]-S-HDL) and near-infrared fluorescence (NIRF, DiD-S-HDL) at 48 hours p.i.

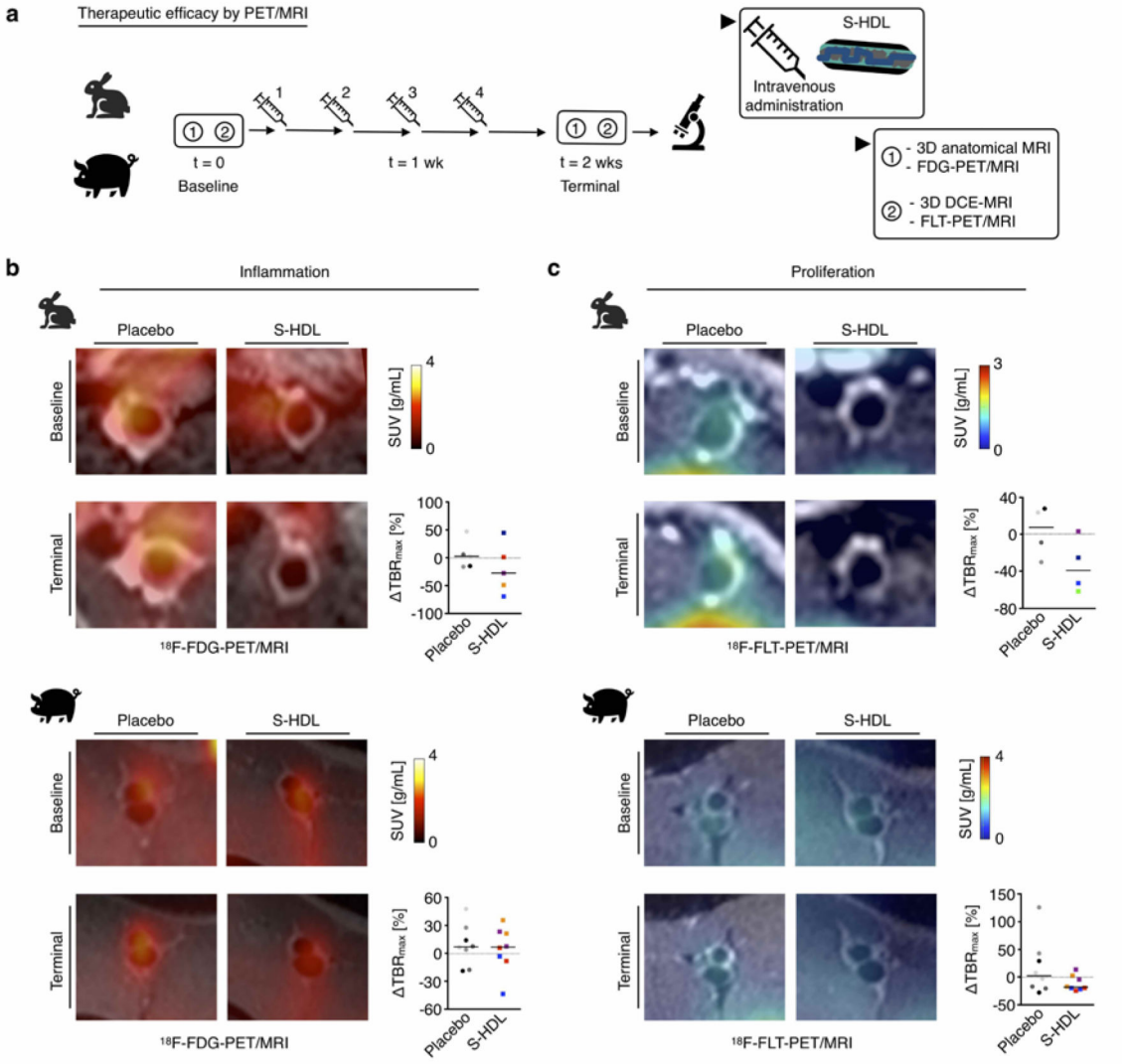

Fig. 3. Imaging-guided S-HDL nanoimmunotherapy in rabbits and pigs. PET-based readouts.

a. Schematic representation of S-HDL imaging-guided treatment. Treatment response was evaluated longitudinally by performing a baseline scan before the first S-HDL administration, and a terminal scan 48 hours after the last one. **b.** ^{18}F-FDG-PET imaging-based assessment of vessel wall inflammation in rabbits (top) and pigs (bottom) treated with PBS (Placebo) or S-HDL. **c.** ^{18}F-FLT-PET imaging-based assessment of cellular proliferation in the vessel wall in rabbits (top) and pigs (bottom) treated with PBS (Placebo) or S-HDL. In panels b and c, dots are color-coded for individual animals, and two data points are represented per pig, corresponding to values obtained from analysis on each of the femoral arteries. Line is situated at median.

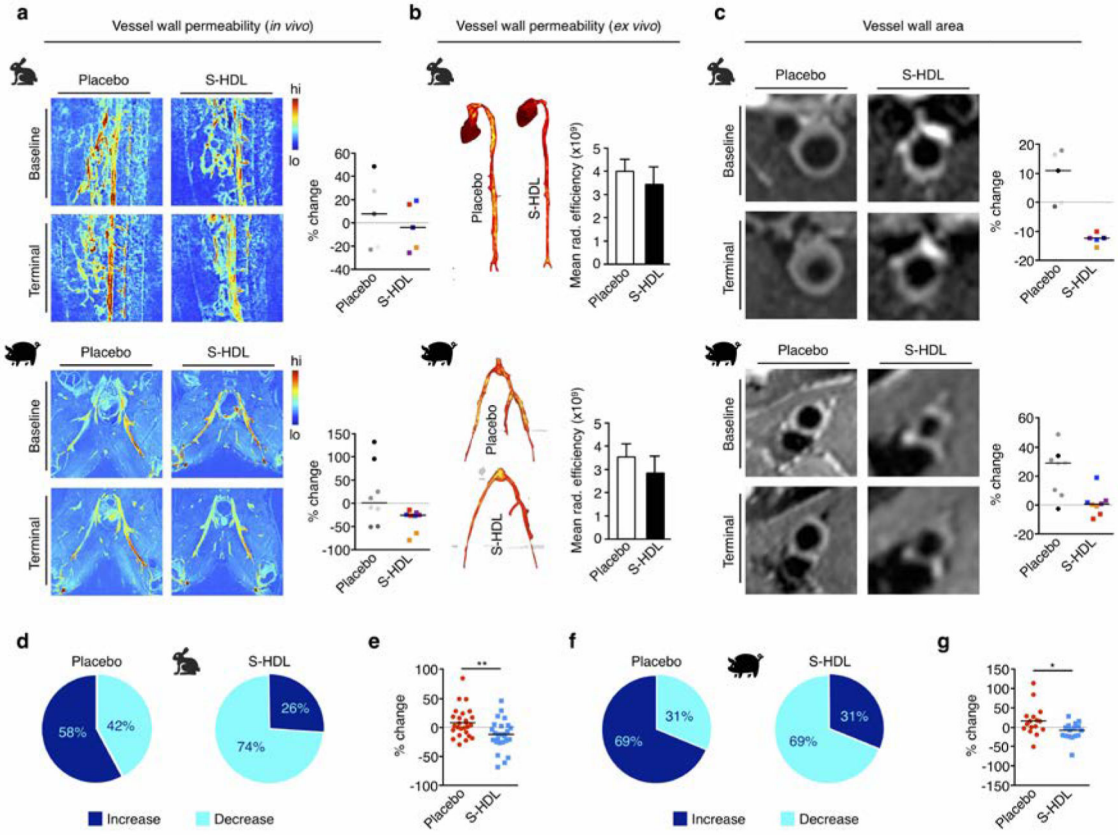

Fig. 4. Imaging-guided S-HDL nanoimmunotherapy in rabbits and pigs. MRI-based readouts.

a. 3D dynamic contrast-enhanced MRI-based vessel wall permeability measurements in rabbits (top) and pigs (bottom) treated with PBS (Placebo) or S-HDL. **b.** *Ex vivo* vessel wall permeability assessed by Evans blue near-infrared fluorescence imaging in rabbit aortas and porcine femoral arteries. **c.** T2-weighted MRI-based vessel wall area measurements in rabbits (top) and pigs (bottom) treated with PBS (Placebo) or S-HDL. In panels a and c, dots are color-coded for individual animals, and two data points are represented per pig, corresponding to values obtained from analysis on each of the femoral arteries. Line is situated at median. **d.** Proportion of scans that afforded increased or decreased imaging marker values in rabbits treated with PBS (Placebo) or S-HDL. **e.** Pooled representation of the variation in the four independent imaging parameters in rabbits treated with PBS (Placebo) or S-HDL (line is situated at median). **f.** Proportion of scans that afforded increased or decreased imaging marker values in pigs treated with PBS (Placebo) or S-HDL. **g.** Pooled representation of the variation in the four independent imaging parameters in pigs treated with PBS (Placebo) or S-HDL (line is situated at median). * $P < 0.05$, ** $P < 0.01$.

Table 1.

Blood biochemistry results from pigs with atherosclerosis treated with PBS (Placebo) or S-HDL. Data are presented as median [interquartile range].

	Placebo	S-HDL	*P*
Alkaline phosphatase (ALP)(U/L)	127 [87–175]	85 [70–132]	0.15
SGPT (ALT)(U/L)	45 [39–67]	51 [38–65]	0.94
SGOT (AST)(U/L)	69 [43–222]	67 [53–160]	0.80
Gamma-glutamyl transferase (GGT)(U/L)	40 [34–78]	41 [39–56]	0.67
Creatine phosphokinase (CPK)(U/L)	740 [406–1817]	796 [431–1024]	0.94
Total bilirubin (mg/dL)	0.2 [0.1–0.2]	0.2 [0.2–0.3]	0.28
- Direct bilirubin (mg/dL)	0.0 [0.0–0.1]	0.0 [0.0–0.1]	>0.99
- Indirect bilirubin (mg/dL)	0.1 [0.1–0.2]	0.2 [0.1–0.3]	0.37
Total protein (g/dL)	6.6 [5.9–6.7]	6.8 [6.5–7.1]	0.21
- Albumin (g/dL)	3.5 [3.4–4.0]	4.0 [3.7–4.5]	0.29
- Globulin (g/dL)	2.6 [2.5–3.1]	2.8 [2.5–2.9]	0.81
- Albumin/Globulin ratio	1.4 [1.2–1.6]	1.4 [1.3–1.8]	0.75
Blood urea nitrogen (BUN)(mg/dL)	12 [10–14]	10 [8.5–17]	0.79
Creatinine (mg/dL)	0.9 [0.8–1.2]	1.0 [0.9–1.2]	0.69
BUN/Creatinine ratio	13 [9.1–17]	11 [9.0–15]	0.94
Glucose (mg/dL)	76 [71–80]	67 [34–69]	**0.03**
Cholesterol (mg/dL)	573 [450–628]	507 [426–747]	0.80
Triglycerides (mg/dL)	62 [26–72]	72 [48–186]	0.31
Sodium (mmol/L)	140 [140–141]	139 [136–141]	0.20
Potassium (mmol/L)	4.4 [4.3–5.1]	4.6 [4.1–7.5]	0.44
Na/K ratio	32 [28–33]	30 [21–35]	0.44
Magnesium (mg/dL)	2.0 [1.9–2.4]	2.1 [1.9–2.8]	0.81
Calcium (mg/dL)	10 [9.4–11]	10 [9.9–10.2]	0.88
Phosphorus (mg/dL)	7.4 [7.2–7.9]	6.9 [6.4–8.6]	0.53
Bicarbonate (mmol/L)	22 [19–24]	19 [17–24]	0.49
Chloride (mmol/L)	99 [98–101]	102 [97–105]	0.49

SGPT = serum glutamic pyruvic transaminase; ALT = alanine aminotransferase; SGOT = serum glutamic-oxaloacetic transaminase; AST = Aspartate aminotransferase.

Table 2.

Complete blood count results from pigs with atherosclerosis treated with PBS (Placebo) or S-HDL. Data are presented as median [interquartile range].

	Placebo	S-HDL	*P*
Red blood cell # (M/μL)	8.1 [6.3–9.7]	5.0 [3.8–6.5]	0.06
Hemoglobin (g/dL)	13 [10–16]	8.9 [7.3–11]	0.19
Hematocrit (%)	43 [32–54]	31 [25–45]	0.29
Mean corpuscular volume (MCV)(fL)	53 [51–56]	66 [62–69]	**0.02**
Mean corpuscular hemoglobin (MCH)(pg)	16 [16–17]	18 [17–19]	**0.03**
MCH concentration (g/dL)	30 [29–31]	28 [26–30]	0.11
Reticulocyte # (K/μL)	27 [20–42]	65 [38–161]	0.06
Reticulocyte (%)	0.28 [0.25–0.60]	1.5 [0.7–3.2]	0.06
Platelet # (K/μL)	175 [142–193]	226 [166–393]	0.19
White blood cell # (K/μL)	6.9 [5.5–9.6]	5.5 [5.2–5.9]	0.25
Neutrophil # (K/μL)	3.3 [2.4–5.2]	1.6 [1.1–2.1]	0.06
Lymphocyte # (K/μL)	3.4 [2.8–3.8]	3.8 [3.1–4.1]	0.68
Monocyte # (K/μL)	0.35 [0.24–0.49]	0.24 [0.17–0.36]	0.26
Eosinophil # (K/μL)	0.08 [0.05–0.16]	0.03 [0.02–0.12]	0.44
Basophil # (K/μL)	0.0 [0.0–0.01]	0.01 [0.0–0.01]	0.52
Neutrophil (%)	51 [41–56]	33 [20–37]	**0.03**
Lymphocyte (%)	41 [39–52]	63 [59–72]	**0.03**
Monocyte (%)	4.4 [3.8–5.9]	4.3 [3.1–6.3]	0.71
Eosinophil (%)	1.0 [0.6–2.1]	0.5 [0.3–2.0]	0.44
Basophil (%)	0.0 [0.0–0.1]	0.2 [0.0–0.2]	0.29